Chemical Papers (2021) 75:2667–2682
https://doi.org/10.1007/s11696-021-01517-x

ORIGINAL PAPER

Pitting corrosion behavior of SS-316L in simulated body fluid and electrochemically assisted deposition of hydroxyapatite coating

Yassine Koumya[1] · Youssef Ait Salam[1] · Mohy Eddine Khadiri[1] · Jaouad Benzakour[1] · Abderrahmane Romane[1] · Abdesselam Abouelfida[1] · Abdelaziz Benyaich[1]

Received: 7 July 2020 / Accepted: 13 January 2021 / Published online: 27 January 2021

Abstract

The pitting corrosion of SS-316L in human body fluid leads the metallic prosthesis to lose its strength along with severe health consequences such as metallosis condition. Hence, an effective alternative for enhancing the biocompatibility of the SS-316L implant is the electrochemical deposition of a bioinert hydroxyapatite (HAP) coating over the metallic surface. A dense HAP coating was successfully developed on SS-316 L in a supersaturated electrolyte containing Ca^{+2} and PO_4^{3-} ions. Electrochemical essays and SEM morphological observation showed the SS-316 L pitting corrosion caused by chloride containing body fluid. The effects of the electrodeposition time and the temperature of the supersaturated electrolyte were assessed using current–time transients, scanning electron microscopy, Energy-dispersive X-ray spectroscopy, Raman and X-ray diffraction analyses. The increase in the temperature promotes the HAP coating formation and accelerates the particles nucleation. An instantaneous HAP growth with no evidence for intermediate phase of HAP formation has been noticed.

Keywords Corrosion · SBF · Hydroxyapatite · PDP · Impedance · Cyclic voltammetry · Current–time transients · SEM · XRD · Raman

Introduction

Due to their corrosion resistance against wet and dry corrosion, austenitic stainless steels are considered most chosen materials for the use in various industrial applications (Vera Cruz et al. 1996). Their corrosion resistance is attributed to the growth of a thin, adherent passive film (e.g., chromium oxide, Cr_2O_3 and iron oxide, Fe_2O_3) which protects the structure against the corrosive environment (Khatak and Raj 2002; Hakiki et al. 1995). The passivity is considered as three dimensional growth of an oxide/hydroxide barrier layer (i.e., impedes the flow of current across the metal solution interface) and its chemical composition depends on the stainless steel alloy and the aggressive environment (Fattah-alhosseini et al. 2011; Gopi et al. 2007; Macdonald 2012; Oguike 2014). Austenitic stainless steels are becoming the mostly widely used materials in the bioimplant manufacturing and their development, to enable the chemical binding to bone, never ceases to grow (Al-Rashidy et al. 2018; Kannan et al. 2005; López et al. 2008). Bioimplants could be divided into two main types: metallic materials (which include titanium alloys, cobalt based alloys, stainless steels, etc.) and inorganic materials such as ceramics and hydroxyapatite (HAP) (Jamesh et al. 2012; Kannan et al. 2004). These materials are typically used to replace or repair a damaged biological structure because of the bone and cartilage disorders or the trauma (Bose and Tarafder 2012; Liu and He 2018). Specifically, 316 L stainless steel (SS-316L) has gained a wide reputation as an implant in reconstructive surgery due to its favorable mechanical and chemical properties. The coated SS-316L remains the metallic implants of a special interest to stabilize a biological structure (e.g., bone tissue) and accelerate the healing process or to replace the damaged biological tissue (Richard et al. 2004).

The corrosion of the metallic biomaterials is a serious health problem which worsens as the combination with mechanical stress increases (e.g., corrosion fatigue and tribocorrosion). Multiple consequences may occur, such as metallosis (i.e., the tissue precipitation of metallic particles, such as cobalt and chromium, owing to the corrosion

✉ Yassine Koumya
koumya.yassine@gmail.com

[1] Laboratory of Applied Chemistry and Biomass, Department of Chemistry, Faculty of Science Semlalia, University Cadi Ayyad, BP 2390, Marrakech, Morocco

of joint prostheses), which can cause an increasingly severe embolisms, allergies, atrophy of certain tissues and chronic tissue reactions. In order to prevent these consequences as early as possible, the metallic biomaterials implanted in the human body should have the potential to generate a stable protective film in salivary environment or aggressive plasma. Hence, the stainless steels, titanium and cobalt-based alloys are most used metallic biomaterials (Richard et al. 2004; Niinomi 2010).

Furthermore, despite the growing importance of titanium and its alloys as orthopaedic implants, SS-316L is very popular because of its relatively low cost, ease of manufacturing and corrosion resistance. However, in the long term, austenitic stainless steels are prone to localized corrosion (i.e., pitting corrosion). As the plasma environment is chloride containing medium, it can promote the pitting corrosion. Generally, the damages such as crack formation and peeling off of the passive film, which results in a local depassivation of the metallic surface, are highly caused by different corrosion forms (such as tribocorrosion) (Richard et al. 2004).

Studies have shown that metallic ions, released by vitro corrosion of austenitic stainless steel, cause the alteration in the action human antigenic lymphocytes and inhibit the immune response, as assessed by cell proliferation. Following on studies conducted on the microanalysis of the corrosion products in the pits vicinity in the SS-316L metallic prosthesis, the enrichment of molybdenum on the surface of the implant is revealed as well as the corrosion products including iron, chromium and nickel metallic ions (Richard et al. 2004; Schmidt 1999).

Because of their excellent bioactivity and bone similarities, calcium phosphates are widely used in bone tissue engineering for hard tissues (i.e., teeth or bone replacement, etc.) (Abbass et al. 2018; Bose and Tarafder 2012; Kannan et al. 2004; Lu et al. 2004; Wang et al. 2010).

Various techniques have been performed to fabricate calcium phosphates (CaP) including thermal spraying techniques (i.e., Plasma spraying, High velocity oxy-fuel spraying), vapor deposition techniques (i.e., Ion beam assisted deposition, Pulsed laser deposition, Magnetron sputtering, Electron-cyclotron-resonance plasma sputtering) and wet techniques (i.e., Electrophoretic deposition, Electrochemical or cathodic deposition, Sol–gel deposition, Wet-chemical and biomimetic deposition, Dip coating, Spin coating, Hydrothermal deposition, Thermal substrate deposition). However, the electrochemically assisted deposition (ECAD) is considered as an effective method for different reasons such as, lower working temperature, the deposition of thin film close to the chemical composition of bone mineral, control of the thickness and chemical composition of coatings, formation of the homogeneous coatings on structured and porous surfaces, and physicochemical stability of the coatings (Azem et al. 2016; Ban and Maruno 1995; Dorozhkin 2015; Jamesh et al. 2012; León and Jansen2009; Lopez-Heredia et al. 2007; Eason 2006). The electrochemically assisted deposition (ECAD) of HAP phases is only achieved with electrically conductive substrates in Ca and P containing electrolytes (León and Jansen 2009). The process is triggered with a cathodic polarization of the substrates which results in the formation of OH^- ions causing the increase in the pH of bulk/substrate interface (Wolf-Brandstetter et al. 2014). Hence, the nucleation of HAP phases is produced in the vicinity of the substrate surface. Although the electrochemical reactions play a major role in the deposition of calcium phosphate phases, the deposition using electrochemically assisted does not imply any transfer in charge carriers in the sense of an electrochemical reaction (Leó and Jansen 2009).

Considering that the implant surface is the main part interacting with the host, different deposits have been produced to improve the materials biocompatibility (Dorozhkin 2015). The electrodeposition of hydroxyapatite on SS-316 L fulfils the requirements of mechanical properties and biocompatibility (Assadian et al. 2015). Cakir et al. reported four types of calcium phosphates coatings synthesized using electrochemical deposition (ED): brushite or dicalcium phosphate dehydrate (DCPD, $CaHPO_4{\cdot}2H_2O$), monetite or dicalcium phosphate anhydrous (DCPA, $CaHPO_4$), octacalcium phosphate (OCP, $Ca_8(HPO_4)_2(PO_4)_4{\cdot}5H_2O$), and hydroxyapatite (HAP, $Ca_{10}(OH)_2(PO_4)_6$) (Azem et al. 2016).

The hydroxyapatite constitutes the major inorganic phases of the human hard tissues (i.e., bone and teeth) (Khatak and Raj 2002; Hakiki et al. 1995; Vera Cruz et al. 1996). It has been proved to be an effective material for large surgical procedure, such as bone replacement, dental defect filling, bone tissue engineering and drug delivery (Chozhanathmisra et al. 2017; Dănăilă and Benea 2016; Gopi et al. 2011, 2013; Kannan et al. 2003, 2004; Mixtures 2019; Souto et al. 2003; Wang et al. 2010; Yoshinari et al. 1994; Yuan and Golden 2009; Zhang et al. 1998, 2018).

Cakir and his colleagues (Azem et al. 2016; Cakir 1985) argued that dicalcium phosphate anhydrous is considered as one of the precursors of hydroxyapatite HAP (e.g., which has similar mineral composition of the human bone). Other researchers concluded that the coating bioactivity and the bone formation are highly related of the dissolution of the precursors such as Ca^{2+} and PO_4^{3-} (Dorozhkin 2011; Lu et al. 2005, 2008).

In this study, we investigate the electrodeposition of HAP phases on SS-316L by applying a cathodic potential at which the hydroxide ions are produced. Firstly, the corrosion behavior SS-316L stainless steel in a simulated biological fluid (SBF) is studied by carrying out the potentiodynamic polarization and electrochemical impedance spectroscopy measurements. Then, the effect of chloride ions on SS-316L implant is thoroughly discussed. For the current–time

transients, a supersaturated solution (SE) buffered at a pH of 5.5 is used for the hydroxyapatite coating deposition. In the second section of the study, the hydroxyapatite growth is discussed as function of saturated electrolyte temperature and electrodeposition time. The growth of HAP coatings was characterized by using scanning electron microscopy (SEM) coupled to EDX analysis, Raman spectroscopy and XRD measurements.

Experimental

Electrochemical experiments

The electrochemical study of SS-316L behavior and HAP electrodeposition was carried out using a regular three-electrode cell assembly consisting of SS-316L as working electrode with a surface area of $1cm^2$; a platinum counter electrode, and a saturated calomel electrode (SCE) serving as a reference electrode.

The pretreatment of samples consisted of mechanical polishing of exposed area with silicon carbide SiC abrasion papers of 500, 1200, 1500, and 2000 grits. Then, they were washed with distilled water, rinsed with acetone, and dried in air before carrying out the electrochemical measurements. The electrochemical cell is controlled by a PGZ 301 potentiostat/galvanostat which is piloted by a computer equipped with Volta Master software that allows the calculation of the electrochemical parameters.

Potentiodynamic Polarization curves (PDP) are recorded at constant sweep rate of 1 mV/s in a scanning range from − 1 V versus SCE to 1.5 V versus SCE.

Before carrying out the PDP experiments, the working electrode was immersed in the test cell for 60 min until attaining steady state. The measurements were repeated three times for each condition to insure the reproducibility. AC electrochemical impedance spectroscopy (EIS) measurements are carried out in frequency range of 100 kHz to 10 MHz with amplitude of 10 mV peak-to-peak using alternating current (AC) signals at open circuit potential (OCP). Double layer capacitance (C_{dl}) and charge transfer resistance (R_{ct}) values are deduced from AC EIS plots.

Study of the corrosion behavior of 316L steel in the SBF environment

Potentiodynamic polarization experiments and electrochemical impedance spectroscopy were used to investigate the corrosion behavior of SS-316L in a biological environment. The electrochemical essays were performed in SBF solution (simulated body fluid), prepared by dissolving given amounts of chemicals listed in Table 1. The pH of the solution was adjusted to 7.4 by adding an amount of NaOH and using a pH meter, the temperature had been fixed at 37 °C.

Supersaturated electrolyte preparation

The electrodes were immersed in a supersaturated electrolyte (SE) which was prepared by dissolving: 0.2839 g Na_2HPO_4, 0.4439 g $CaCl_2$ and 8 g NaCl, in distilled water. Then, the pH of the supersatured electrolyte was buffered at 5.5. The buffered solutions were used for HAP deposition. A volume of 100 mL of supersaturated electrolyte acid is used to ensure the proper immersion of electrodes in the cylindrical Pyrex glass cell. In order to perform the EIS experiments at steady state, the stirrer rotational speed was set at 180 rpm and at controlled temperature of 37 °C using a bath thermostat.

Prior to electrodeposition, cyclic voltammetry measurements were carried out to determine the potential to be applied for electrodeposition. Current time transients were carried out for the HAP electrodeposition. In this electrochemical deposition, both hydrogen gas and hydroxide ions were produced on the SS-316L surface being the cathode.

Results

Study of the corrosion behavior of 316L steel in the SBF environment

Open circuit potential The SS-316L was immersed in the SBF medium and was allowed to evolve thermodynamically as function of time before reaching a steady state.

Figure 1 illustrates the evolution of the open circuit potential of SS-316L as function of time. The potential is changed from initial value of − 360.64 mV to the more negative value of − 366.09 mV and then reached a stable value. The first open circuit potential fluctuations before 30 min of electrode immersion (Fig. 1, inset), is typical for the competition between the passive film growth and the breakdown of the passivity (Strehblow 1984). The corrosion resistance of SS-316L is generally attributed to the formation of a chromium oxide (Cr_2O_3) based passive film upon contact with aggressive environment (Gaben et al. 2004). The potential shift toward the negative direction could be linked to chloride ions effect, which often slow down the repassivation of metastable pits and stimulates their stability.

Table 1 The quantities of chemicals used for the preparation of SBF solution (1L)

NaCl	$NaHCO_3$	KCl	K_2HPO_4	$MgCl_2$	HCl (1 M)	$CaCl_2$	Na_2SO_4
7.996 g	0.350 g	0.224 g	0.228 g	0.305 g	40 mL	0.278 g	0.071 g

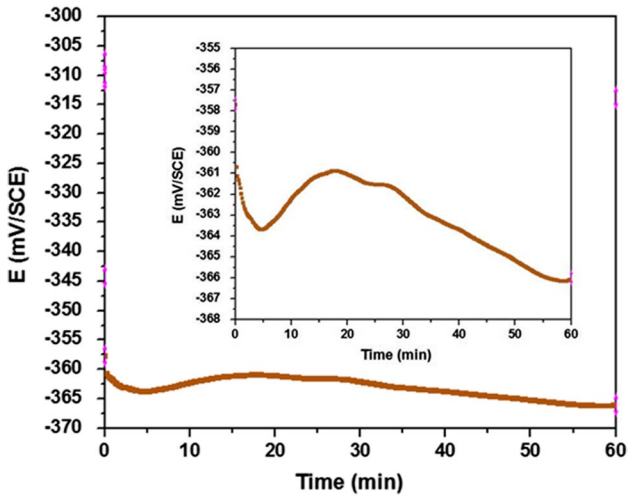

Fig. 1 Open circuit potential as function of time for 316L steel immersed in the SBF solution at a temperature of 37 °C and a pH = 7.4. The inset indicates a zoomed view of the potential fluctuation versus immersion time

Potentiodynamic polarization (PDP) Potentiodynamic polarization essays were performed out using a scan rate of 1 mV/s commencing at a potential about − 1 V more cathodic than the OCP. Before the PDP scan, SS-316L was left in the cell for about 60 min to attain a steady state**.** The corrosion behavior of SS-316L in SBF was compared to the SS-316L corrosion in sulfuric acid in order to discuss the pitting potential displacement. The pitting potential is regarded as the point where the current increases suddenly without dropping to passive current again (Xu et al. 2018).

As for SBF medium, we note that the passivation width is narrowed as shown in Fig. 2. The the passive plateau ranges from 0.58 V/SCE to 0.12 V/SCE, before passivity

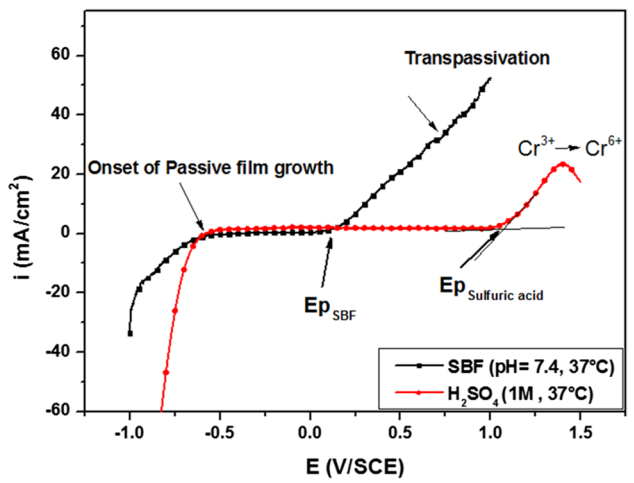

Fig. 2 Potentiodynamic polarization curves for SS-316L in SBF medium and sulfuric acid 1 M at 37 °C

was broken due to pitting corrosion. Table 2 lists the electrochemical parameters of the SS-316L corrosion in SBF and sulfuric acid. The pitting potential (Ep) of SS-316L in SBF is around 100 mV/SCE, while that of SS-316L in sulfuric acid is far higher. It is found that there is a very little variation in corrosion potential when comparing the effect of both media on the kinetic behavior of SS-316L general corrosion. The corrosion potential of SS-316L corrosion, in SBF and sulfuric acid, does not vary as much as the pitting potential. This is consistent with the pronounced effect of chloride ions, contained in the SBF solution, on the pitting corrosion of the stainless steel.

This fact could be justified by the pitting corrosion of SS-316L in SBF due to the presence of high content of chloride ions. As for SBF solution, the potentiodynamic polarization curve does not display the onset of the abrupt increase in current density of Cr^{3+} oxidation to Cr^{6+}.

In sulfuric acid, the Cr (III) oxide being oxidized to Cr (VI) leads most likely to the pit initiation due to the increase in the local acidity as described by this equation (Koumya et al. 2019):

$$2Cr^{3+} + 7H_2O \rightarrow Cr_2O_7^{2-} + 14H^+ + 6e^- \quad (1)$$

Even so, the pitting mechanism of SS-316L stainless steel is still blurry. The pitting corrosion of wrought stainless steels always initiates at the inclusions (Man et al. 2019).

Man et al. held that the pitting potential of 316L SS manufactured by selective laser melting was about 0.205 V higher than that of the wrought SS-316L in SBF, indicating that there was a significant difference in their pitting corrosion behavior (Man et al. 2019). Sander et al. (Sander et al. 2017) contended that the pitting potential of SLM 316L stainless steel was about 0.3 V higher than that of the wrought sample. It was discussed that sample porosity and the agressiveness of the medium are responsible for this pitting potential difference. In the work of Talha et al. (Talha et al. 2012), the high pitting corrosion susceptibility of type 316L was due to surface passive film with less protective to reveal high anodic dissolution rate.

Figure 2 illustrates the evolution of the current density as a function of the SS-316L potential in SBF medium (pH = 7.4 at 37 °C).

Lopez et al. have reported that, in the range of potentials studied, SS-316L shows evidence of pitting corrosion

Table 2 Electrochemical parameters for SS-316L in SBF (pH 7.4) and sulfuric acid 1 M at 37 °C

	E_{corr} (mV/SCE)	E_{pit} (V/SCE)
SBF	− 480	0.100
H_2SO_4 1M	− 581	1.056

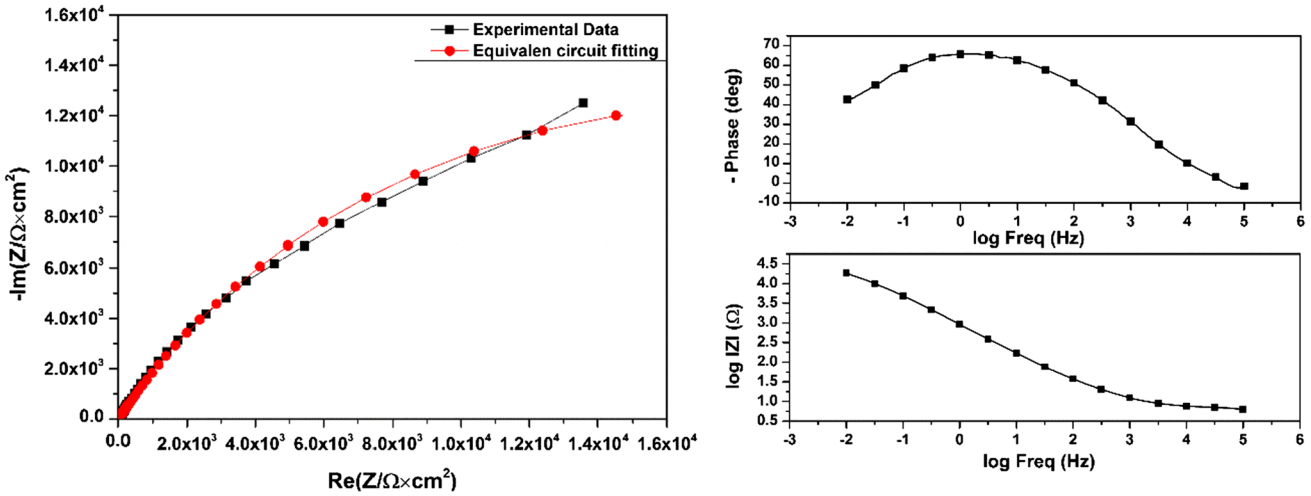

Fig. 3 Nyquist and bode plots obtained for untreated SS-316L in SBF at 37 °C

Table 3 Impedance fitting values of SS-316L corrosion in SBF using equivalent circuit

R_1 (Ω×cm^2)	Q_2 (μF×S^{a-1}×cm^{-2})	a_2	R_2 (kΩ×cm^2)
6.998	288	0.717	45.131

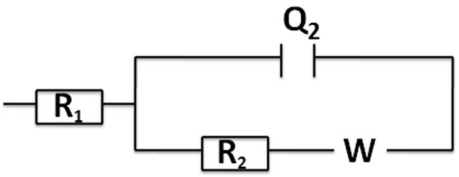

Fig. 4 Equivalent circuits for fitting SS316L corrosion in SBF medium

(López et al. 2008). It was discussed that in neutral solutions, the passive film is usually composed of a chromium-rich inner layer and an iron-rich outer layer. In these conditions the passive film thickens basically because of iron oxides. However, in acidic solutions a chromium-rich oxide film is formed due to the slower dissolution of Cr oxides compared to Fe oxides (López et al. 2008). Malik et al. (Malik et al. 1992) have studied the influence of pH and chloride concentration on the corrosion behaviour of SS-316 l steel in aqueous solutions. They argued that, at a particular chloride concentration, a critical pitting potential (E_{pit}) develops which is sufficient to displace oxygen from the protective oxide layer.

Electrochemical impedance spectroscopy The uncoated SS-316L sample, immersed in SBF solution at 37 °C, was also evaluated by EIS in order to identify the different time constants and processes involved in the corrosion mechanism. Nyquist and bode plots, obtained for untreated SS-316L in SBF at 37 °C, are presented in Fig. 3. the corresponding electrochemical parameters are listed in Table 3. This metal/solution interface is described using Nyquist diagrams, where the imaginary part of impedance is plotted as a function of real part. The Bode plot shows the total impedance |Z| and phase angle θ, as a function of frequency.

Figure 3 reveals that the Nyquist plot is characterized by an incomplete capacitive loop representative of the charge transfer owing to the high charge transfer resistance (R_{ct} = 45.13 kΩ×cm^2). At the lower frequencies, the Warburg impedance is used to model the increasing ionic conductivity due to the diffusivity in the passive film. No slope change in the Bode diagram |Z| versus frequency is observed, thus, the interface is described by one time constant in series Warburg impedance as the slope of the plot |Z| versus frequency is near − 1/2. The diffusion process is observed at the lower frequencies due to the circulation of the electrolyte to reach the metal surface.

Among the equivalent circuits most reported in the literature for the SS-316L corrosion in SBF, the equivalent circuit, given in Fig. 4, describes well the interface of the SS-316L in the studied experimental conditions.

A purely capacitive impedance will have a phase angle of − 90°, thus a constant phase element (CPE) was introduced to mimic a non-ideal dielectric behavior because of the phase angle that does not reach − 70°. Besides, Nyquist plot is depressed due to the uneven current distribution at metal/surface interface caused by the surface inhomogeneities at the electrode surface at nano/micro scale (e.g., roughness, porosity, adsorption, and/or diffusion).

Jorcin et al. (2006) reported that the impedance data for a solid electrode/electrolyte interface often reveal a

frequency dispersion that cannot be described by simple elements such as resistances, capacitances, inductances or convective diffusion (e.g., Warburg impedance). Therefore, the frequency dispersion is generally attributed to a capacitance dispersion expressed in terms of a constant-phase element (CPE). According to Fricke, the time constant dispersion is the most often the result of the capacity dispersion or to a change of the capacity with frequency (Fricke 1932).

Different equations were discussed in the literature concerning the CPE impedance (Brug et al. 1984; Łosiewicz et al. 2004). Lasia (1993) gives the impedance of the CPE as:

$Z_{CPE} = 1/(Q\ (j\omega)^{a})$, where Q is a CPE constant in F S^{a-1} cm^{-2} and a is related to the angle of rotation of a purely capacitive line on the complex plane. j is the imaginary number, and is the angular frequency ($\omega = 2\pi f$, f being the frequency).

The physical cencept of CPE is not clear since different origin of the capacitance distribution have been discussed on the literature such as: Surface roughness, heterogeneities, electrode porosity, variation of coating composition, slow adsorption reaction, nonuniform potential and current distribution (Córdoba-Torres et al. 2012; Hirschorn et al. 2010; Huang et al. 2007; Jorcin et al. 2006).

The large semicircle diameter indicates a very high corrosion resistance for the high frequency RC time constant (Hermas and Morad 2008). The obtained equivalent circuit contains one constant phase element to consider the one relaxation time constant. The CPE parameter ($a_2 = 0.71$) is intermediate between the Warburg impedance ($a = 0.5$) and the capacitor ($n = 1$).

In SBF containing chloride ions, the following mechanism could be suggested:

$$Fe + H_2O + Cl^- \leftrightarrow [FeClOH]^-_{ads} + e^- \quad (2)$$

$$[FeClOH]^-_{ads} \leftrightarrow [FeClOH]_{ads} + e^-(rds) \quad (3)$$

$$[FeClOH] + H^+ \leftrightarrow Fe^{2+} + Cl^- + H_2O \quad (4)$$

where $[FeClOH]_{ads}$ is the adsorbed intermediate that is involved in the rate determining step of SS-316L dissolution in SBF.

It should be noted that SBF is a chloride containing biological fluid resulting often in SS-316L pitting corrosion. The concentration of chloride ions at the interface SS-316L/SBF is consistently at a high level because of chloride containing SBF solution. Cl^- ions can weaken the passive film formed on the surface of metal and penetrate through the corrosion product layer, thus forming soluble corrosion product (Qichao Zhang et al. 2019).

Electrochemical deposition of hydroxyapatite phases on SS-316L

Determination of the potential of the cathodic polarization Prior to the chronoamperometric electrodeposition of the hydroxyapatite HAP on the SS-316L, a cyclic voltammetry study is required to determine the potential at which the hydroxyapatite deposits are grown. To avoid any electrochemical reaction resulting from the oxidation of the SS-316L, we have used a platinum electrode as working electrode. Cyclic voltammetry measurements were performed in the saturated electrolytic medium (SE), the potentiostat is set to sweep forward from −2 to 2 V and then sweep back from 2 to −2 V with respect to the reference electrode. Figure 5 shows cyclic voltammograms recorded at different scan rates in the saturated electrolytic medium (SE).

CVs depicted in Fig. 5 reveal that the intensity of the anodic and cathodic peaks is proportional to the scan rate. It should be noted that as the scan rate goes higher, the peaks become more observable.

Two reduction peaks are observed, one of which corresponds to the production of OH^- ions which are the driving force for the formation of hydroxyapatite deposits on the surface of SS-316L. These ions were produced by reduction of water H_2O at a potential of − 1.36 V/SCE. The cathodic potential of H_2O reduction will be applied in the next chronoamperometric essays for the hydroxyapatite electrodeposition. To understand the kinetics governing the H_2O reduction, we have plotted the current density of the cathodic peak as a function of the square root of the scan rate (Fig. 6).

Figure 6 shows a linear relationship between the cathodic water reduction and the square root of scan rate. We note that

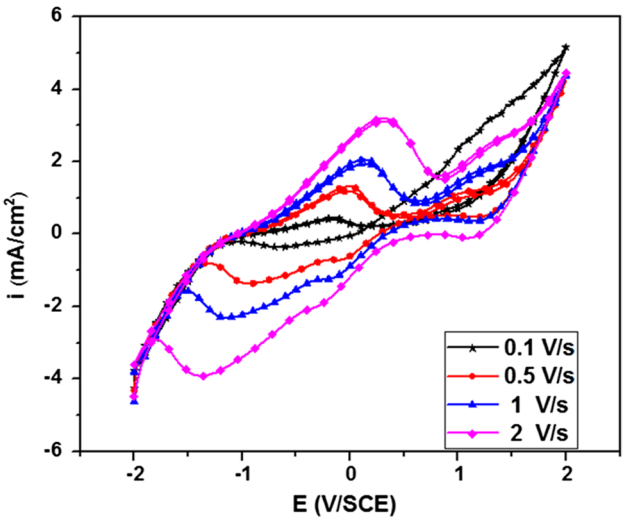

Fig. 5 Cyclic voltammograms (CVs) recorded at different scan rates in the saturated electrolytic medium (SE) using platinum working electrode

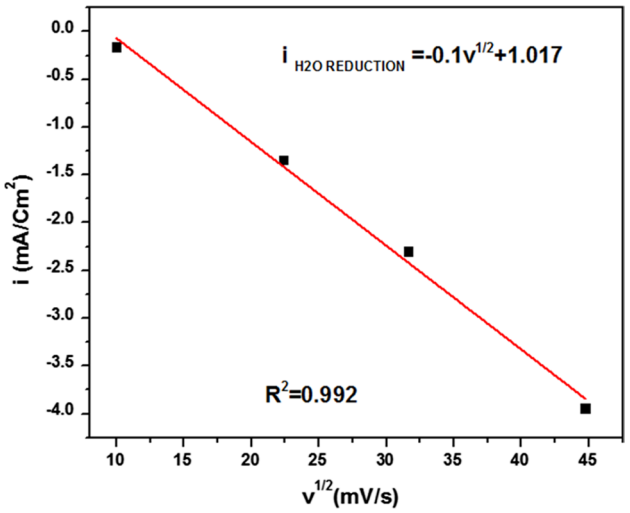

Fig. 6 Current density of the H_2O reduction as a function of the square root of the scan rate in a saturated electrolyte medium (SE)

the peak current increases with the scan rate. According to Cottrell equation (Myland and Oldham 2004), in the fast electron transfer process, the peak current is proportional to the square root of the scan rate. This relationship may be related to a semi-infinite linear diffusion behavior that dominates the cathodic reaction (Lord et al. 2010). According to Berzins-Delahay equation, this linear relation suggests that the cathodic reaction is a diffusion-controlled process (Peng et al. 2016).

The chronoamperometric method has been carried out for the electrodeposition of HAP coatings. This electrochemical method is based on the cathodic release of hydroxide ions in vicinity of the SS-316L surface and therefore the adhesion of HAP on metallic surface.

Electrodeposition of HAP as function of the process time The electrochemical deposition of HAP coatings on SS-316L is described by the following equations, these chemical reactions are occurring in the vicinity of the SS-316L (cathode) electrode. This following reaction reveals that the local pH on the cathode surface is increased relative to bulk electrodeposition solution as result of the water reduction (Peng et al. 2006).

$$2H_2O + 2e^- \leftrightarrow H_2 + 2OH^- \tag{5}$$

The hydroxide ions engaged in the following acid–base reactions lead to an increase in the local phosphate ion concentration:

$$OH^- + H_2PO_4^- \leftrightarrow HPO_4^{2-} + H_2O \tag{6}$$

$$HPO_4^{2-} + OH^- \leftrightarrow PO_4^{3-} + H_2O \tag{7}$$

The following precipitation reactions should be taken into account:

$$10Ca^{2+} + 6PO_4^{3-} + 2OH^- \leftrightarrow Ca_{10}(PO_4)_6(OH)_2 \tag{8}$$

$$3Ca^{2+} + 2PO_4^{3-} + nH_2O \leftrightarrow Ca_3(PO_4)_2 * nH_2O \tag{9}$$

$$8Ca^{2+} + 6HPO_4^{2-} + 5H_2O \leftrightarrow Ca_8H_2(PO_4)_6 * 5H_2O + 4H^+ \tag{10}$$

$$Ca^{2+} + HPO_4^{2-} + 2H_2O \leftrightarrow CaHPO_4 + 2H_2O \tag{11}$$

According to these electrochemical/chemical reactions, CaP phases precipitate over the SS-316L surface and therefore lead to the formation of a thin coating on the stainless-steel cathode. Peng et al. reported different factors affecting the coating fabrication such as stirring rate, distance between the working and counter electrodes, and amplitude of applied voltage and pulse frequency (Peng et al. 2006). According to the literature, the transport of electroactive species (HPO_4^{2-} ions) occurs through hemispherical diffusion regions developed around each single nucleus. However, the hemispherical diffusion radius of these rays increases with time. During this stage, the transport of electroactive species (HPO_4^{2-} ions) to nuclei formed on the surface occurs through hemispherical diffusion zones developed around each individual nucleus (Katic et al. 2013). However, as the time goes by, the radius of these hemispherical diffusion zones increases due to the nuclei growth, and the zones start to overlap, which ultimately leads to forming a planar diffusion zone (Katic et al. 2013).

Gopi et al. (2011) studied the electrodeposition of hydroxyapatite onto borate passivated surgical grade stainless steel. It has been demonstrated that as the constant value of potential, used for electrochemical deposition, increased to − 1400 mV/SCE, hydroxyapatite became the major phase of deposits. It is demonstrated that the electrochemical deposition results in an increasing pH at the interface due to electron incorporation to form OH^- ions and H_2 through water reduction. As excess OH^- is produced, HAP can be deposited on the cathode surface by the following reaction:

$$10Ca^{2+} + 6PO_4^{3-} + 2OH^- \leftrightarrow Ca_{10}(PO_4)_6(OH)_2 \tag{12}$$

It has been revealed that the fabrication of HAP at high potentials (− 1600 mV/SCE) generates reaction bubbles in the vicinity of the electrode which affects the uniformity of calcium phosphate deposition. Therefore, it was demonstrated that the electrodeposition at − 1400 mV/SCEis the most suitable potential to obtain a uniform coating on SS-316L (Gopi et al. 2011).

Scanning Electron Microscopy (SEM)

The surface morphology of as prepared coatings fabricated at different immersion times were investigated on a TESCAN VEGA3 SEM (accelerating voltage 20 kV). After conducting current time transient assays, the SS-316L samples were taken out of the cell and cleaned with deionised water, and then dried for SEM analyses**.** Figure 7 shows the SEM morphology of SS-316L coatings fabricated at different immersion times (magnification 1.00 k).

For the immersion of the uncoated SS-316L in SBF, we note that the surface is highly pitted owing to chloride containing SBF, the surface appears the presence of different pits on the sample surface along with some scratches because of the surface polishing. It can be seen that local sites have been attacked owning to the most obvious localized corrosion. Chloride being a relatively small anion with high diffusivity interferes and penetrates toward the passive film causing deleterious effects (Balamurugan et al. 2006). Figure 8-a shows many uncovered pits over the SS-316L surface, indicating that the most metastable pits initiated in SS-316L surface were converted within less than 1 h to stable pits (Sander et al. 2017).

Figures 7 and 8 show that the SS-316L appears a completely covered surface for the period of 30 min, However, for long period of immersion, the deposits are intense in some areas but not over the entire alloy surface.

The micrographs of hydroxyapatite coated 316L steel for different immersion times indicate that the dense deposit is obtained for short immersion times. The corresponding EDX data (a), (b) and (c) shown in Table 4 reveal the hydroxyapatite elements (Ca, P and O) of the deposit, and also the elements of the substrate due to the fact that the surface is not completely covered.

The decrease in the percentage of the Fe, Cr and Ni of the substrate as shown in Table 4 undoubtedly evinces that the substrate surface is coated with HAP which prevents the detection of SS-316L alloying elements. There are also some percentages related to the Cl and Na for different coatings, which come from the electrolyte solution.

As shown in Figs. 7 et 8, the dense and uniform coatings are observed for the short period of electrodeposition. As for 30 min of electrodeposition, we observe different electrodeposited phases corresponding to the nucleation and growth of hydroxyapatite crystals. The weak deposits observed at long periods could be explained by the release of the pre-adsorbed HAP layer with long periods of immersion.

The high carbon percentage of the deposited coating at 1 h and 3 h may be attributed to the formation of the carbonate apatite of low crystallinity as the temperature

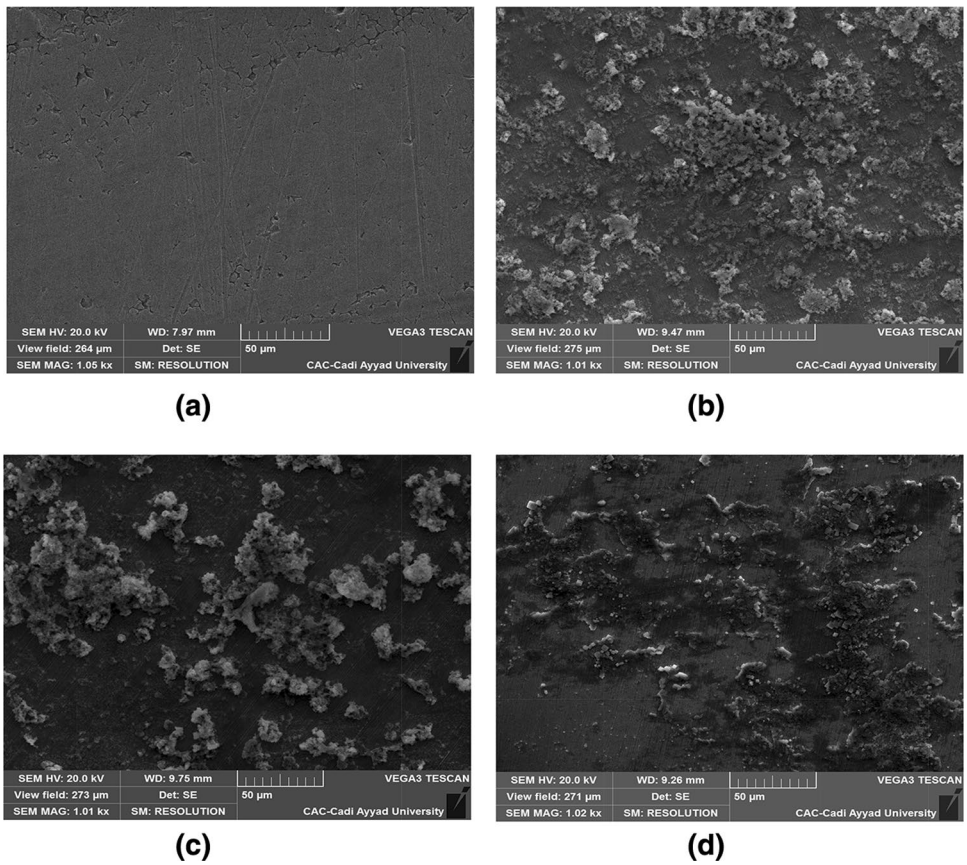

Fig. 7 SEM micrographs of the electrodeposited HAP coating on SS-316L as function of time: **a** immersed uncoated SS-316L in SBF for 24 h, **b** 30 min HAP electrodeposition, **c** 1 h HAP electrodeposition, **d** 3 h HAP electrodeposition

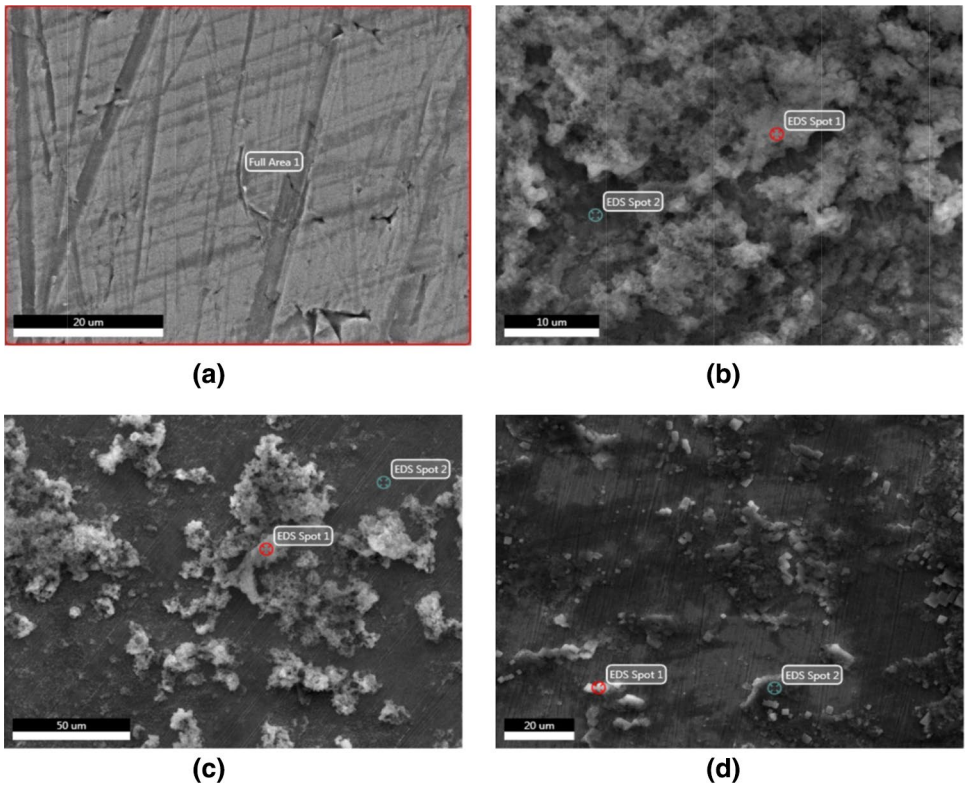

Fig. 8 Magnified SEM micrographs of the electrodeposited HAP coating on SS-316L as function of time: **a** immersed uncoated SS-316L in SBF for 24 h, **b** 30 min HAP electrodeposition, **c** 1 h HAP electrodeposition, **d** 3 h HAP electrodeposition

Table 4 EDX mass percentage of the electrodeposited HAP coating on SS-316L as function of time: (a) immersed uncoated SS-316L in SBF for 24 h, (b) 30 min HAP electrodeposition, (c):1 h HAP electrodeposition, (d): 3 h HAP electrodeposition

Element	(a)	(b)		(c)		(d)	
		Spot1	Spot2	Spot1	Spot2	Spot1	Spot2
Fe	63.26	5.85	28.64	2.72	65.19	7.83	18.35
Cr	16.89	1.88	8.39	0.74	17.74	2.28	5.28
Ni	9.96	–	3.89	0.18	10.18	1.01	2.53
Na	–	20.61	21.52	6.55	–	36.53	24.68
Cl	–	20.88	13.00	7.64	–	26.26	17.10
C	4.67	–	–	44.31	3.44	14.21	19.13
O	1.21	24.53	10.38	23.91	–	8.81	8.21
Ca	–	17.20	8.25	6.82	0.41	1.02	2.04
P	–	9.04	5.13	4.10	0.14	0.85	1.35

of SE medium increases. Previous studies demonstrated that calcium phosphate coatings on titanium plate by the electrochemical method in a simulated body fluid were carbonated calcium phosphates with low crystallinity (Ban and Maruno 1995),

In the work of Al-Rashidy et al. on the orthopedic bioactive glass/chitosan composites coated 316L stainless steel by green electrophoretic co-deposition, it has been demonstrated the formation of newly carbonated HA layer (Al-Rashidy et al. 2018).

Effect of temperature on the electrodeposition of HAP particles

Current time transients Figure 9 shows the current time transients corresponding to the HAP electrodeposition on SS-316L as function of SE temperature, performed a constant potential of − 1.36 V/SCE for one hour at a pH of 5.5. The resulting current time transients are a typical response of an electrochemical nucleation and growth of HAP layers. Two stages of HAP production are occurring: In the first

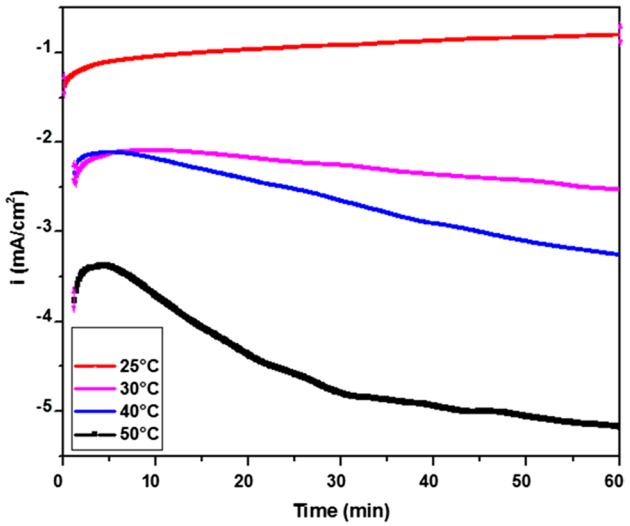

Fig. 9 Current time transients for HAP coating formed on SS-316L in SE obtained by applying a potential of − 1.36 V/SCE for duration of 60 min at different temperatures

stage, the nucleation of the HAP over the SS-316L as evidenced by the increase in the current density. Then, the current density reaches a constant value indicating the growth of HAP phases resulting in forming a dense layer. As for 30 and 40 °C, we note a very slow nucleation kinetic as the stable current density value is not reached. The current density value reached after one hour decreases with increasing temperature (at 50 °C, $i_{max} = -3.5$ mA/cm^2).

The shape of current–time transients observed is characteristic of nucleation and growth processes of HAP. The rapid increase in current density at very short time is explained by the growth of new HAP nuclei. The coalescence of the neighboring diffusion fields with localized spherical symmetry generates a maximum current density. The decay of current density may be ascribed to a planar electrode diffusion (Peng et al. 2016; Scharifker and Hills 1983). Katic asserted that during the nucleation stage, the transport of electroactive species (HPO_4^{2-} ions) to nuclei formed on the surface occurs through hemispherical diffusion zones developed around each individual nucleus (Peng et al. 2016).

Morphological characterizations of the coatings

SEM morphological analysis SEM micrographs (Fig. 10) clearly indicate the growth of HAP phases over the SS-316L for all studied electrochemical deposition. As the temperature increases, we note a dense agglomerates of calcium phosphate (Ca–P) with a clumped distribution over the sam-

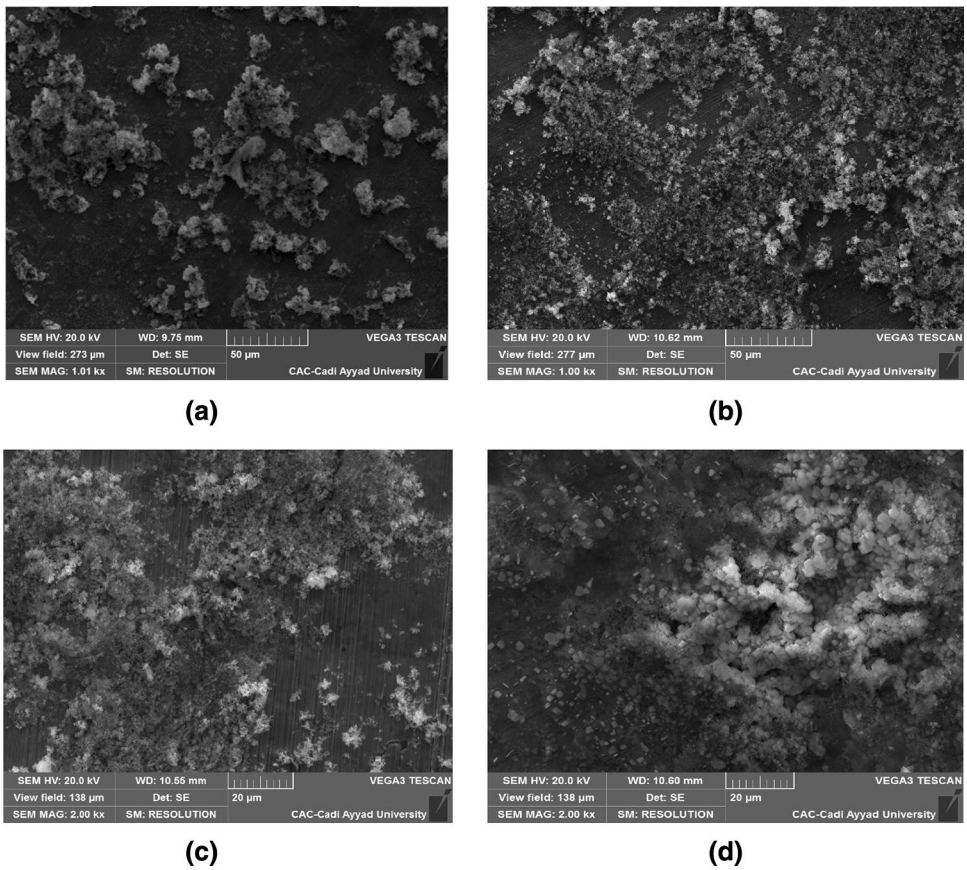

Fig. 10 SEM micrographs of electrodeposited HAP coating on SS-316L as function of temeprature: **a** 25 °C, **b** 30 °C, **c** 40 °C, **d** 50 °C

Table 5 EDX mass percentage of electrodeposited HAP coating on SS-316L as function of temperature: (a) 25 °C, (b) 30 °C, (c) 40 °C, (d) 50 °C

Element	(a)		(b)	(c)	(d)	
	Spot1	Spot2	Full area	Full area	Spot1	Spot2
Fe	5.85	28.64	30.28	36.73	1.55	28.12
Cr	1.88	8.39	8.67	10.38	0.56	8.09
Ni	–	3.89	4.08	5.09	–	3.90
Na	20.61	21.52	9.85	13.90	33.67	6.46
Cl	20.88	13.00	4.92	7.57	34.47	8.68
C	–	–	3.44	3.10	–	1.31
O	24.53	10.38	16.55	9.40	4.75	6.65
Ca	17.20	8.25	13.42	7.47	16.34	24.66
P	9.04	5.13	7.95	4.88	8.11	11.12

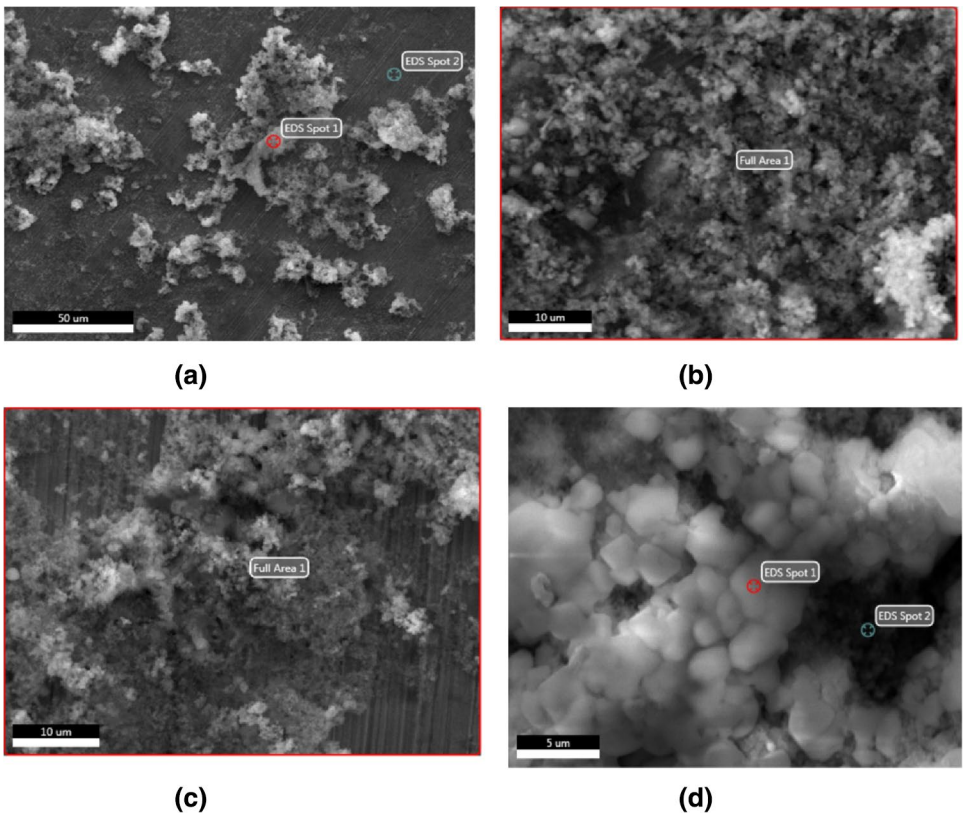

Fig. 11 Magnified SEM micrographs of electrodeposited HAP coating on SS-316L as function of temperature: **a** 25 °C, **b** 30 °C, **c** 40 °C, **d** 50 °C

ple surface. These results are corroborated with mass percentage of HAP elements (Ca, P and O) as listed in Table 5. It should be noted that substrate surface exhibits dense coating as the temperature attains to 50 °C. Figure 11d illustrates that the SS-316L surface is highly covered with agglomerated HAP particles (i.e., dense and uniform precipitation). The surface has more white clumped spherical clusters related to the supersaturated solution precursors as shown by the EDX listed in Table 5. The increase in the mass percentage of the elements Na, Cl, Ca, P and O evidences clearly the reinforced HAP coating with the temperature increase. In contrast, for 25 °C, the SS surface appears so many bare surfaces regions with a local HAP growth. The SEM micrographs prove that the deposited coating has two distinctive regions: conductive substrate surface and non-conductive area of hydroxyapatite agglomerates. The brightness of the non-conductive coating of HAP results from the HAP's feature to hold the electric charge, while the conductive areas of SS-316L bare surface remains relatively darker. The micrograph of HAP electrodeposition at 50 °C, as shown in Fig. 11-d, depicts a bright grain-like particles with a size ranging from almost 2 and 5 µm. Whereas, The HAP particles size seems to be decreased compared to the other electrodeposition temperatures as no particles are clearly distinguished at the magnified images despite the fact that the micrographs are taken at the magnified scale.

The magnified SEM micrographs of SS-316L surface at different temperatures of electrochemical deposition are presented in Fig. 11. The spherical shaped particles (white areas) observed in the micrographs, obtained for 50 °C, are due to the presence of Na and Cl resulting from the dissolved precursors such as Na_2HPO_4, $CaCl_2$, NaCl. The spot elemental analysis of the coating fabricated at 50° shows the decrease in the mass percentage of the SS-316L alloying elements (e.g., Fe, Ni, Cr) compared to the studied temperatures (Table 5-d).

The high Ca to P mass ratio calculated using the EDS mass percentage was obtained for the local analysis of the HAP coating fabricated at 50 °C: Ca/P mass ratio is around 2.21 for spot 1 at 50 °C, whereas for all temperatures does not exceed the threshold of 2. Although the electrodeposited HAP coating is relatively bonded uniformly, the temperature increase leads to improve the adhesion and the bonding strength of the HAP coating.

Ben et al. investigated the electrodeposition of calcium phosphate coatings in SBF medium. It was shown an amorphous growth of the coating at 5, 22 and 37 °C. Whereas, those formed at 52 and 62 °C contained $Mg(OH)_2$, $CaCO_3$ and carbone apatite of low cristallinity. It is concluded that the diffusion process is a rate determining step in the electrochemical synthesis of calcium phosphate in the studied temperatures (Ban and Maruno 1995).

Thanh et al. (Thanh et al. 2013) held that the deposition temperature can affect the hydroxyapatite by the change in the reaction rate as well as the diffusion rate of ions. It was explained that the high temperatures result in high diffusion rates which promote the growth of HAP coating or the bulk precipitation. Their results are in good agreement with the present findings. Moreover, as the temperature increases, the coating deposition is favored with the accelerated particles nucleation. However, they stated that, for a high adhesive strength between the coating and the substrate, the HAP electrodeposition should be performed at lower temperatures to decrease the hydrogen bubble on the substrate (Drevet et al. 2018; Lopez-Heredia et al. 2007; Thanh et al. 2013; Zhang et al. 2005).

Raman spectroscopy

Raman spectra were recorded in raman spectroscopy (Confotec MR520) with laser of wavelength ($\lambda = 532$ nm). Raman analysis was carried out to identify the formation of hydroxyapatite on the surface of SS-316L samples. Figure 12 illustrates the different spectra obtained using Raman spectroscopy analysis at different temperatures. The corresponding positions and allocations of the different peaks are gathered in Table 6.

Raman spectra for uncoated substrate and as synthesized HAP/SS-316L at different temperatures are shown in Fig. 12. Different characteristic peaks are observed: a characteristic ν_1 (PO_4), ν_2 (PO_4), three peaks ν_3 (PO_4) and a peak ν_4 (PO_4). All these bands were assigned to the internal vibration modes of the phosphate groups. There is also a single intense band that is attributed to the hydroxide ions of hydroxyapatite $\nu 5$ (OH) at 2920 cm^{-1}. As evident from Fig. 12, the high intensity of characteristic peaks ν_1 (PO_4), ν_2 (PO_4), ν_4 (PO_4) and ν_5 (OH) is associated with the as received coating synthesized at 30 °C. At 50 °C. It is clearly seen that the HAP characteristic are very low. These results seem to substantiate the SEM micrographs obtained for various temperatures of electrodeposition. Therefore, there is evidence to suggest that the adsorbed HAP content decreased with increasing the electrochemical deposition temperature. In other words, the high temperature of the deposition solution medium could have influenced the adhesion of the HAP coating and results in the pre-adsorbed HAP phases. The electrodeposition of HAP at all studied temperatures shows an instantaneous HAP growth as there is no evidence for intermediate phase growth of HAP. Ren

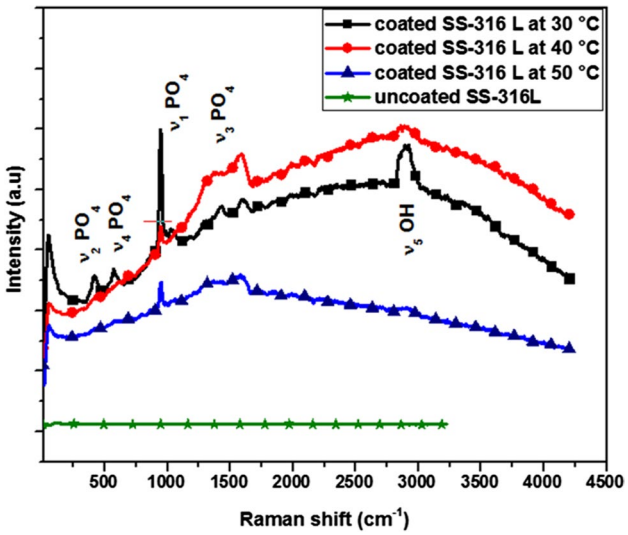

Fig. 12 Raman spectra for uncoated substrate and as synthesized HAP/SS-316L at different temperatures

Table 6 Raman shift and attribution of the HAP electrodeposition on SS-316L as function of temperature

Raman shift (cm^{-1})	Attribution
420	ν_2 PO_4
576	ν_4 PO_4
946	ν_1 PO_4
1432	ν_3 PO_4
1604	
1700	
2920	ν_5 OH

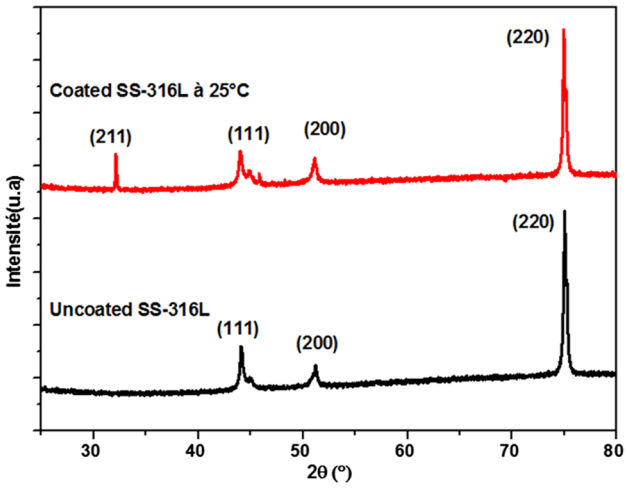

Fig. 13 XRD patterns of uncoated substrate and the HAP coating on SS-316L

et al. have studied the electrochemical deposition mechanism of calcium phosphate coating in dilute Ca-P electrolyte system, they have proved the direct deposition of HAP with no intermediates (Hu et al. 2009).

X-ray diffraction (XRD)

To study the HAP growth on SS-316L substrates, the as received samples were analyzed by X-Ray diffraction (Rigaku, Cu Kα1, $\lambda = 1.5418$ Å). Figure 13 illustrates X-ray diffraction patterns for uncoated substrate and electrodeposited HAP coating on SS-316L for 1 h at 25 °C. The XRD patterns indicated that the coatings were composed of an apatitic phase with a low crystallinity.

Figure 13 illustrates the XRD pattern of the uncoated SS-316L and the HAP coating on substrate using potentiostatic deposition for 1 h at − 1.36 V/ECS. The XRD patterns show the presence of three well resolved peaks for the uncoated substrate, located at $2\theta = 44°$, $2\theta = 51°$ and $2\theta = 75°$, corresponding, respectively, to the crystalline planes (111), (200) and (220). According to the literature, these are the characteristic peaks of 316L stainless steel, which can be attributed to iron, chromium and nickel (i.e., Fe, CrO, FeO, NiO) (Thanh et al. 2013). The diffractogram of HAP coated SS-316L displays a characteristic peak related to the HAP coating, resolved at $2\theta = 32°$ corresponding to the crystal plane (211) which is characteristic of hydroxyapatite crystals according to the standard JCPDSN° 01-073-0293. Many authors reported the crystal plane (211) resolved almost at 30° as a typical XRD peak of HAP coating. Thanh et al. reported a second HAP characteristic peak at $2\theta \sim 26°$ corresponding to the (002) crystalline plane. Different authors found that the diffraction peak (002) is the strongest peak in the XRD pattern, therefore, concluded that the HAP crystals grow perpendicularly to the substrate surface (c-direction) (Prado Da Silva et al. 2001; Rusu et al. 2005).

Conclusions

Out of this study it can be stated that:

The present study seeks to discuss the electrochemical deposition of HAP coating on SS-316L as function of the electrodeposition time and temperature. The potentiodynamic polarization study showed that the pitting potential of SS-316L in SBF was more negative than that of sulfuric acid 1 M. SEM study confirmed that the simulated body fluid promotes many stable pits.

For the chronoamperometric electrodeposition of HAP, a cathodic potential of -1.36 V/SCE, corresponding to the OH^- release, was determined to be an effective potential. A dense coating is observed for the short period of electrodeposition. At high temperature (i.e., 50 °C), the current time transient showed the characteristics of nucleation and growth of HAP phases. SEM morphological analysis revealed highly agglomerated clusters of HAP. The increase in the temperature promotes the HAP coating formation and accelerates the particles nucleation. The as-grown coating on the SS-316L substrates were characterized using Raman and XRD analyses. Different characteristic peaks of HAP were observed with the increase in the Raman intensity as the supersaturated solution temperature increases. XRD corroborated the previous findings and suggested the formation of low crystallized HAP phases.

Compliance with ethical standards

Conflict of interest The authors confirm that there are no known conflicts of interest associated with this publication and there has been no significant financial support for this work.

References

Abbass MK, Ajeel SA, Wadullah HM (2018) Biocompatibility, bioactivity and corrosion resistance of stainless steel 316L nanocoated with TiO_2 and Al_2O_3 by atomic layer deposition method. J Phys Conf Ser. https://doi.org/10.1088/1742-6596/1032/1/012017

Al-Rashidy ZM, Farag MM, Abdel Ghany NA, Ibrahim AM, Abdel-Fattah WI (2018) Orthopaedic bioactive glass/chitosan composites coated 316L stainless steel by green electrophoretic co-deposition. Surf Coat Technol 334:479–490. https://doi.org/10.1016/j.surfcoat.2017.11.052

Assadian M, RezazadehShirdar M, Idris MH, Izman S, Almasi D, Taheri MM, Abdul Kadir MR (2015) Optimisation of electrophoretic deposition parameters in coating of metallic substrate by hydroxyapatite using response surface methodology. Arabian J SciEng 40(3):923–933. https://doi.org/10.1007/s13369-014-1544-2

Azem FA, Delice TK, Ungan G, Cakir A (2016) Investigation of duty cycle effect on corrosion properties of electrodeposited calcium

phosphate coatings. Mater SciEng C 68:681–686. https://doi.org/10.1016/j.msec.2016.06.010
Balamurugan A, Balossier G, Kannan S, Rajeswari S (2006) Elaboration of sol-gel derived apatite films on surgical grade stainless steel for biomedical applications. Mater Lett 60(17–18):2288–2293. https://doi.org/10.1016/j.matlet.2005.12.126
Ban S, Maruno S (1995) Effect of temperature on electrochemical deposition of calcium phosphate coatings in a simulated body fluid. Biomaterials 16(13):977–981. https://doi.org/10.1016/0142-9612(95)94904-Y
Bose S, Tarafder S (2012) Calcium phosphate ceramic systems in growth factor and drug delivery for bone tissue engineering: a review. ActaBiomater 8(4):1401–1421. https://doi.org/10.1016/j.actbio.2011.11.017
Brug GJ, van den Eeden ALG, Sluyters-Rehbach M, Sluyters JH (1984) The analysis of electrode impedances complicated by the presence of a constant phase element. J ElectroanalChem Interfacial Electrochem 176(1–2):275–295. https://doi.org/10.1016/S0022-0728(84)80324-1
Cakir A (1985) Induction time and reactivation of passive films on iron. ElectrochimActa 30(4):551–557. https://doi.org/10.1016/0013-4686(85)80046-3
Caroline R, Martine W, Bernard Normand NP (2004) Prévention et lutte contre la corrosion: une approche scientifique et technique (P. polytechniques et universitaires Romandes (ed.)). Presses polytechniques et universitaires romandes
Chozhanathmisra M, Murugan N, Karthikeyan P, Sathishkumar S, Anbarasu G, Rajavel R (2017) Development of antibacterial activity and corrosion resistance properties of electrodeposition of mineralized hydroxyapatite coated on titanium alloy for biomedical applications. Mater Today Proc 4(13):12393–12400. https://doi.org/10.1016/j.matpr.2017.10.009
Córdoba-Torres P, Mesquita TJ, Devos O, Tribollet B, Roche V, Nogueira RP (2012) On the intrinsic coupling between constant-phase element parameters α and Q in electrochemical impedance spectroscopy. ElectrochimActa 72:172–178. https://doi.org/10.1016/j.electacta.2012.04.020
Dănăilă E, Benea L (2016) Comparative tribocorrosion resistance in physiological solution of untreated and modified Ti–6Al–4V alloy surface by electrodeposition of hydroxyapatite coatings into nanoporoustitania layers. Adv Mater Res 1139:64–68. https://doi.org/10.4028/www.scientific.net/amr.1139.64
Dorozhkin SV (2011) Calcium orthophosphates: occurrence, properties, biomineralization, pathological calcification and biomimetic applications. Biomatter 1(2):121–164. https://doi.org/10.4161/biom.18790
Dorozhkin SV (2015) Calcium orthophosphate deposits: preparation, properties and biomedical applications. Mater SciEng C 55:272–326. https://doi.org/10.1016/j.msec.2015.05.033
Drevet R, Zhukova Y, Kadirov P, Dubinskiy S, Kazakbiev A, Pustov Y, Prokoshkin S (2018) Tunable corrosion behavior of calcium phosphate coated Fe–Mn–Si alloys for bone implant applications. Metall Mater Trans A 49(12):6553–6560. https://doi.org/10.1007/s11661-018-4907-6
Eason R (2006) Pulsed laser deposition of thin films. Wiley, New York. https://doi.org/10.1002/0470052120
Fattah-alhosseini A, Soltani F, Shirsalimi F, Ezadi B, Attarzadeh N (2011) The semiconducting properties of passive films formed on AISI 316 L and AISI 321 stainless steels: a test of the point defect model (PDM). CorrosSci 53(10):3186–3192. https://doi.org/10.1016/j.corsci.2011.05.063
Fricke H (1932) The theory of electrolytic polarization. Lond Edinburgh Dublin Philos Mag J Sci 14(90):310–318. https://doi.org/10.1080/14786443209462064
Gaben F, Vuillemin B, Oltra R (2004) Influence of the chemical composition and electronic structure of passive films grown on 316L SS on their transient electrochemical behavior. J ElectrochemSoc 151(11):B595–B604. https://doi.org/10.1149/1.1803562
Gopi D, Manimozhi S, Govindaraju KM, Manisankar P, Rajeswari S (2007) Surface and electrochemical characterization of pitting corrosion behaviour of 304 stainless steel in ground water media. J ApplElectrochem 37(4):439–449. https://doi.org/10.1007/s10800-006-9274-0
Gopi D, Prakash CA, V., Kavitha, L., Kannan, S., Bhalaji, P. R., Shinyjoy, E., & Ferreira, J. M. F. (2011) A facile electrodeposition of hydroxyapatite onto borate passivated surgical grade stainless steel. CorrosSci 53(6):2328–2334. https://doi.org/10.1016/j.corsci.2011.03.018
Gopi D, Bhuvaneshwari N, Indira J, Kanimozhi K, Kavitha L (2013) A novel green template assisted synthesis of hydroxyapatite nanorods and their spectral characterization. SpectrochimActa Part A MolBiomolSpectrosc 107:196–202. https://doi.org/10.1016/j.saa.2013.01.052
Hakiki NB, Boudin S, Rondot B, Da Cunha Belo M (1995) The electronic structure of passive films formed o n stainless steels. CorrosSci 37(11):1809–1822. https://doi.org/10.1016/0010-938X(95)00084-W
Hermas AA, Morad MS (2008) A comparative study on the corrosion behaviour of 304 austenitic stainless steel in sulfamic and sulfuric acid solutions. Corros Sci 50:2710–2717. https://doi.org/10.1016/j.corsci.2008.06.029
Hirschorn B, Orazem ME, Tribollet B, Vivier V, Frateur I, Musiani M (2010) Determination of effective capacitance and film thickness from constant-phase-element parameters. ElectrochimActa 55(21):6218–6227. https://doi.org/10.1016/j.electacta.2009.10.065
Hu R, Lin C, Shi H, Wang H (2009) Electrochemical deposition mechanism of calcium phosphate coating in dilute Ca-P electrolyte system. Mater ChemPhys 115(2–3):718–723. https://doi.org/10.1016/j.matchemphys.2009.02.022
Huang VM-W, Vivier V, Orazem ME, Pébère N, Tribollet B (2007) The apparent constant-phase-element behavior of a disk electrode with faradaic reactions. J ElectrochemSoc 154(2):C99. https://doi.org/10.1149/1.2398894
Jamesh M, Kumar S, Narayanan TSNS (2012) Electrodeposition of hydroxyapatite coating on magnesium for biomedical applications. J Coat Technol Res 9(4):495–502. https://doi.org/10.1007/s11998-011-9382-6
Jorcin J-B, Pébère N, Tribollet B (2006) CPE analysis by local electrochemical impedance spectroscopy. ElectrochimActa 51(8–9):1473–1479. https://doi.org/10.1016/J.ELECTACTA.2005.02.128
Kannan S, Balamurugan A, Rajeswari S (2003) Hydroxyapatite coatings on sulfuric acid treated type 316L SS and its electrochemical behaviour in Ringer's solution. Mater Lett 57(16–17):2382–2389. https://doi.org/10.1016/S0167-577X(02)01239-9
Kannan S, Balamurugan A, Rajeswari S (2004) H2SO4 as a passivating medium on the localised corrosion resistance of surgical 316L SS metallic implant and its effect on hydroxyapatite coatings. ElectrochimActa 49(15):2395–2403. https://doi.org/10.1016/j.electacta.2004.01.003
Kannan S, Balamurugan A, Rajeswari S (2005) Electrochemical characterization of hydroxyapatite coatings on HNO_3passivated 316L SS for implant applications. ElectrochimActa 50(10):2065–2072. https://doi.org/10.1016/j.electacta.2004.09.015
Katic J, Metiko-Hukovic M, Babic R (2013) Nitinol modified by calcium phosphate coatings prepared by sol-gel and electrodeposition methods. ECS Trans 53(19):83–93. https://doi.org/10.1149/05319.0083ecst
Khatak HS, Raj B (2002) Corrosion of austenitic stainless steels mechanism mitigation and monitoring WOODHEAD. Woodhead publishing, New York

Koumya Y, Idouhli R, Khadiri M, Abouelfida A, Aityoub A, Benyaich A, Romane A (2019) Pitting corrosion and effect of Euphorbia echinus extract on the corrosion behavior of AISI 321 stainless steel in chlorinated acid. Corros Rev 37(3):259–271. https://doi.org/10.1515/corrrev-2018-0090

Lasia A (1993) Study of electrode activities towards the hydrogen evolution reaction by a.c. impedance spectroscopy. Int J Hydrogen Energy 18(7):557–560. https://doi.org/10.1016/0360-3199(93)90174-9

Leó B, Jansen JA (2009) Thin calcium phosphate coatings for medical implants. In: León B, Jansen J (eds) Thin calcium phosphate coatings for medical implants. Springer, New York. https://doi.org/10.1007/978-0-387-77718-4

León B, Jansen J (2009) Thin calcium phosphate coatings for medical implants. Springer, New York. https://doi.org/10.1007/978-0-387-77718-4

Liu C, He H (2018) Developments and applications of calcium phosphate bone cements, vol 9. Springer, Singapore. https://doi.org/10.1007/978-981-10-5975-9

López DA, Durán A, Ceré SM (2008) Electrochemical characterization of AISI 316L stainless steel in contact with simulated body fluid under infection conditions. J Mater Sci Mater Med 19(5):2137–2144. https://doi.org/10.1007/s10856-007-3138-y

Lopez-Heredia MA, Weiss P, Layrolle P (2007) An electrodeposition method of calcium phosphate coatings on titanium alloy. J Mater Sci Mater Med 18(2):381–390. https://doi.org/10.1007/s10856-006-0703-8

Lord HL, Zhan W, Pawliszyn J (2010) Fundamentals and applications of needle trap devices. Anal ChimActa 677(1):3–18. https://doi.org/10.1016/j.aca.2010.06.020

Łosiewicz B, Budniok A, Rówiński E, Łagiewka E, Lasia A (2004) The structure, morphology and electrochemical impedance study of the hydrogen evolution reaction on the modified nickel electrodes. Int J Hydrogen Energy 29(2):145–157. https://doi.org/10.1016/S0360-3199(03)00096-X

Lu YP, Li MS, Li ST, Wang ZG, Zhu RF (2004) Plasma-sprayed hydroxyapatite+titania composite bond coat for hydroxyapatite coating on titanium substrate. Biomaterials 25(18):4393–4403. https://doi.org/10.1016/j.biomaterials.2003.10.092

Lu X, Zhao Z, Leng Y (2005) Calcium phosphate crystal growth under controlled atmosphere in electrochemical deposition. J Cryst Growth 284(3–4):506–516. https://doi.org/10.1016/j.jcrysgro.2005.07.032

Lu X, Leng Y, Zhang Q (2008) Electrochemical deposition of octacalcium phosphate micro-fiber/chitosan composite coatings on titanium substrates. Surf Coat Technol 202(13):3142–3147. https://doi.org/10.1016/j.surfcoat.2007.11.024

Macdonald DD (2012) Some personal adventures in passivity—a review of the point defect model for film growth. Russ J Electrochem 48(3):235–258. https://doi.org/10.1134/S1023193512030068

Malik AU, Mayan Kutty PC, Siddiqi NA, Andijani IN, Ahmed S (1992) The influence of pH and chloride concentration on the corrosion behaviour of AISI 316L steel in aqueous solutions. CorrosSci 33(11):1809–1827. https://doi.org/10.1016/0010-938X(92)90011-Q

Man C, Dong C, Liu T, Kong D, Wang D, Li X (2019) The enhancement of microstructure on the passive and pitting behaviors of selective laser melting 316L SS in simulated body fluid. Appl Surf Sci 467–468:193–205. https://doi.org/10.1016/j.apsusc.2018.10.150

Mixtures N (2019) Laser surface alloying of 316L stainless steel coated with a bioactive hydroxyapatite-titanium oxide composite laser surface alloying of 316L Stainless Steel with Ru and Ni Mixtures. Int J Corros 2019(46):1–6. https://doi.org/10.1155/2012/162425

Myland JC, Oldham KB (2004) Cottrell's equation revisited: an intuitive, but unreliable, novel approach to the tracking of electrochemical diffusion. ElectrochemCommun 6(4):344–350. https://doi.org/10.1016/j.elecom.2004.01.013

Niinomi M (2010) Metals for biomedical devices. Woodhead publishing, New York

Oguike RS (2014) Corrosion studies on stainless steel (FE6956) in hydrochloric acid solution. Adv Mater PhysChem 04(08):153–163. https://doi.org/10.4236/ampc.2014.48018

Peng P, Kumar S, Voelcker NH, Szili E, Smart RSC, Griesser HJ (2006) Thin calcium phosphate coatings on titanium by electrochemical deposition in modified simulated body fluid. J Biomed Mater Res Part A 76(2):347–355. https://doi.org/10.1002/jbm.a.30514

Peng F, Qin S-J, Zhao Y, Pan G-B (2016) Zn electrodeposition on single-crystal GaN(0001) surface: nucleation and growth mechanism. Int J Electrochem 2016(0001):1–8. https://doi.org/10.1155/2016/3212703

Prado Da Silva MH, Lima JHC, Soares GA, Elias CN, De Andrade MC, Best SM, Gibson IR (2001) Transformation of monetite to hydroxyapatite in bioactive coatings on titanium. Surf Coat Technol 137(2–3):270–276. https://doi.org/10.1016/S0257-8972(00)01125-7

Rusu VM, Ng CH, Wilke M, Tiersch B, Fratzl P, Peter MG (2005) Size-controlled hydroxyapatite nanoparticles as self-organized organic-inorganic composite materials. Biomaterials 26(26):5414–5426. https://doi.org/10.1016/j.biomaterials.2005.01.051

Sander G, Thomas S, Cruz V, Jurg M, Birbilis N, Gao X, Brameld M, Hutchinson CR (2017) On the corrosion and metastable pitting characteristics of 316L stainless steel produced by selective laser melting. J ElectrochemSoc 164(6):C250–C257. https://doi.org/10.1149/2.0551706jes

Scharifker B, Hills G (1983) Theoretical and experimental studies of multiple nucleation. ElectrochimActa 28(7):879–889. https://doi.org/10.1016/0013-4686(83)85163-9

Schmidt R (1999) Comportement des matériaux dans les milieux biologiques: applications. In: PP Romandes (ed). Romandes, Presses Polytechniques. https://books.google.co.ma/books?id=dhQFpcaXg0kC&pg=PA290&lpg=PA290&dq=produits+de+corrosion+tissus+osseux&source=bl&ots=4DhA19Anz7&sig=ACfU3U2hM19L8XGhWp3VQs4Yu0ovc9QGkA&hl=fr&sa=X&ved=2ahUKEwjUma_gpa7qAhXtZhUIHXMoBYkQ6AEwAHoECAoQAQ#v=onepage&q=produits

Souto RM, Laz MM, Reis RL (2003) Degradation characteristics of hydroxyapatite coatings on orthopaedic TiAlV in simulated physiological media investigated by electrochemical impedance spectroscopy. Biomaterials 24(23):4213–4221. https://doi.org/10.1016/S0142-9612(03)00362-4

Strehblow H-H (1984) Breakdown of passivity and localized corrosion: Theoretical concepts and fundamental experimental results. Mater CorrosWerkstoffe Und Korrosion 35(10):437–448. https://doi.org/10.1002/maco.19840351002

Talha M, Behera CK, Sinha OP (2012) Potentiodynamic polarization study of Type 316L and 316LVM stainless steels for surgical implants in simulated body fluids. J Chem Pharm Res 4(1):203–208

Thanh DTM, Nam PT, Phuong NT, Que LX, Anh NV, Hoang T, Lam TD (2013) Controlling the electrodeposition, morphology and structure of hydroxyapatite coating on 316L stainless steel. Mater SciEng C 33(4):2037–2045. https://doi.org/10.1016/j.msec.2013.01.018

Vera Cruz RP, Nishikata A, Tsuru T (1996) AC impedance monitoring of pitting corrosion of stainless steel under a wet-dry cyclic condition in chloride-containing environment. CorrosSci 38(8):1397–1406. https://doi.org/10.1016/0010-938X(96)00028-5

Wang HX, Guan SK, Wang X, Ren CX, Wang LG (2010) In vitro degradation and mechanical integrity of Mg-Zn-Ca alloy coated

with Ca-deficient hydroxyapatite by the pulse electrodeposition process. ActaBiomater 6(5):1743–1748. https://doi.org/10.1016/j.actbio.2009.12.009

Wolf-Brandstetter C, Oswald S, Bierbaum S, Wiesmann HP, Scharnweber D (2014) Influence of pulse ratio on codeposition of copper species with calcium phosphate coatings on titanium by means of electrochemically assisted deposition. J Biomed Mater Res Part B ApplBiomater 102(1):160–172. https://doi.org/10.1002/jbm.b.32992

Xu W, Yu F, Yang L, Zhang B, Hou B, Li Y (2018) Accelerated corrosion of 316L stainless steel in simulated body fluids in the presence of H_2O_2 and albumin. Mater SciEng C 92(2017):11–19. https://doi.org/10.1016/j.msec.2018.06.023

Yoshinari M, Ohtsuka Y, Dérand T (1994) Thin hydroxyapatite coating produced by the ion beam dynamic mixing method. Biomaterials 15(7):529–535. https://doi.org/10.1016/0142-9612(94)90019-1

Yuan Q, Golden TD (2009) Electrochemical study of hydroxyapatite coatings on stainless steel substrates. Thin Solid Films 518(1):55–60. https://doi.org/10.1016/j.tsf.2009.06.029

Zhang JM, Lin CJ, Feng ZD, Tian ZW (1998) Hydroxyapatite/metal composite coatings prepared by two-step electrodeposition method. Chin ChemLett 9(4):403–406

Zhang Q, Leng Y, Xin R (2005) A comparative study of electrochemical deposition and biomimetic deposition of calcium phosphate on porous titanium. Biomaterials 26(16):2857–2865. https://doi.org/10.1016/j.biomaterials.2004.08.016

Zhang L, Zhu F, Li H, Zhao F, Li S (2018) A duplex coating composed of electrophoretic deposited graphene oxide inner-layer and electrodeposited graphene oxide/Mg substituted hydroxyapatite outer-layer on carbon/carbon composites for biomedical application. Ceram Int 44(17):21229–21237. https://doi.org/10.1016/j.ceramint.2018.08.169

Zhang Q, Zheng M, Huang Y, Kunte HJ, Wang X, Liu Y, Zheng C (2019) Long term corrosion estimation of carbon steel, titanium and its alloy in backfill material of compacted bentonite for nuclear waste repository. Sci Rep 9(1):1–18. https://doi.org/10.1038/s41598-019-39751-9